Electronic Supplementary Material (ESI) for Physical Chemistry Chemical Physics.

Assessing Cluster Models of Solvation for the Description of Vibrational Circular Dichroism Spectra: Synergy between Static and Dynamic Approaches

Katia Le Barbu-Debus,[a)] Jessica Bowles,[b)] Sascha Jähnigen,[c)] Carine Clavaguéra,[b)] Florent Calvo,[d)] Rodolphe Vuilleumier,[c)] Anne Zehnacker [a)]

- a) *Institut des Sciences Moléculaires d'Orsay (ISMO), CNRS, Université Paris-Saclay, F-91405 Orsay, France*
- b) *Université Paris-Saclay, CNRS, Institut de Chimie Physique, UMR8000, 91405 Orsay, France*
- c) *PASTEUR, Département de Chimie, Ecole Normale Supérieure, PSL University, Sorbonne Université, CNRS, 75005 Paris, France*
- d) *Université Grenoble Alpes, CNRS, LiPhy, F-38000 Grenoble, France*

Supplementary Information

	E_0	E_0 +ZPE	ΔG
bi-**eq**g$^+$ G$^-$	0.0	0.0	0.0
mono$_{OH}$-**eq**g$^-$G$^-$	3.3	2.0	1.4
mono$_{OH}$-**eq**g$^-$G$^+$	5.3	4.3	2.0
mono$_{OH}$-**eq**tG$^-$	3.9	3.3	2.4
mono$_{OH}$-**eq**g$^-$T	6.2	5.0	3.4
noHB-**eq**g$^+$G$^+$	26.4	22.9	3.4
bi-**eq**g$^+$T	3.1	2.9	4.1
mono$_{OH}$-**ax**g$^+$T	9.4	8.2	4.7
mono$_{OH}$-**eq**tT	7.7	7.4	6.8
mono$_{NH}$-**eq**g$^+$G$^+$	17.6	15.8	10.8
mono$_{OH}$-**eq**g$^+$G$^+$	4.0	3.5	12.7
mono$_{OH}$-**ax**tG$^-$	11.9	11.7	13.7
mono$_{OH}$-**ax**tT	15.2	14.5	16.2

Table S1: Comparison between electronic energies E_0 at 0 K, ZPE-corrected electronic energies at 0 K (kJ/mol) E_0 +ZPE, and Gibbs free energies ΔG at room temperature, for the most stable 1-1 complexes calculated at the B3LYP/6-311++G(d,p) level.

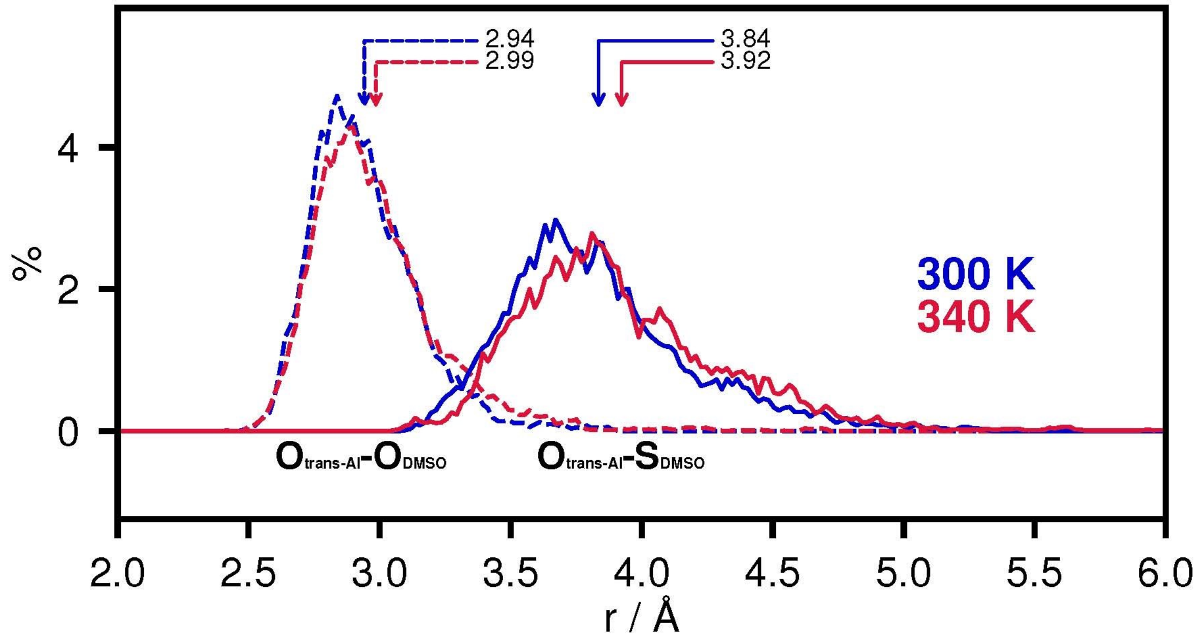

Figure S1: Distribution of distance between the oxygen atom of trans-AI and the oxygen/sulfur atom of DMSO, obtained from the FPMD trajectories at different temperatures (BLYP-D3).

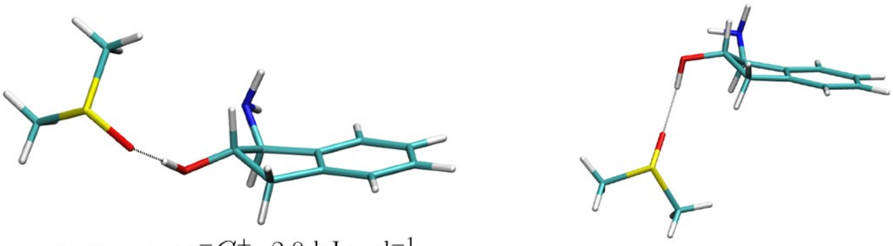

mono_{OH}-$\mathbf{eq}\,g^{-}G^{+}$: 2.0 kJ·mol^{-1}

mono_{OH}-$\mathbf{eq}\,tG^{-}$: 2.4 kJ·mol^{-1}

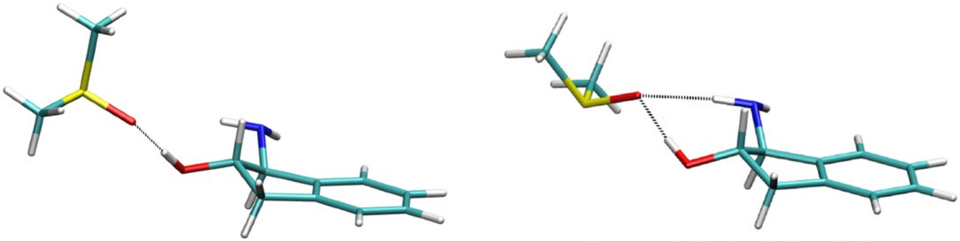

mono_{OH}-$\mathbf{eq}\,g^{-}T$: 3.4 kJ·mol^{-1}

bi-$\mathbf{eq}\,g^{+}T$: 4.1 kJ·mol^{-1}

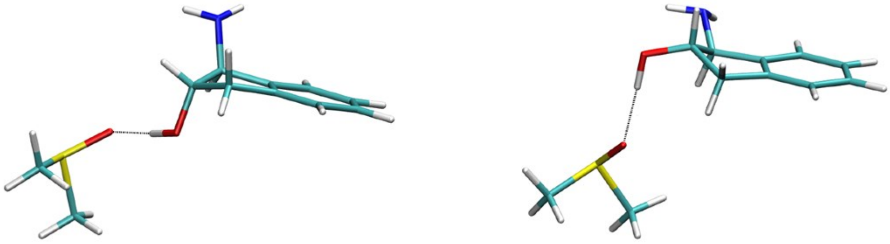

mono_{OH}-$\mathbf{ax}\,g^{+}T$: 4.7 kJ·mol^{-1}

mono_{OH}-$\mathbf{eq}\,tT$: 6.8 kJ·mol^{-1}

mono_{NH}-$\mathbf{eq}\,g^{+}G^{+}$: 10.8 kJ·mol^{-1}

mono_{OH}-$\mathbf{ax}\,tG^{-}$: 13.7 kJ·mol^{-1}

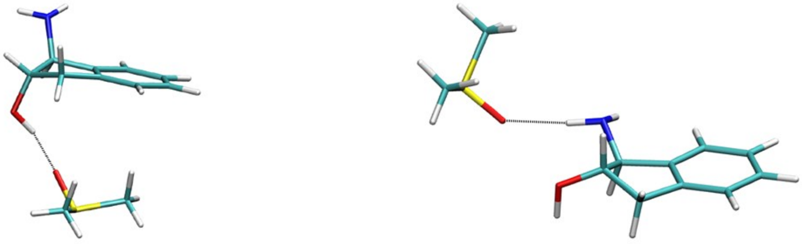

mono_{OH}-$\mathbf{ax}\,tT$: 16.2 kJ·mol^{-1}

mono_{NH}-$\mathbf{eq}\,tT$: 20.8 kJ·mol^{-1}

Figure S2: Stable calculated structure of the *trans*-AI:DMSOd_6 1:1 complex at the B3LYP/6-311G++(d,p) level in a DMSO continuum.

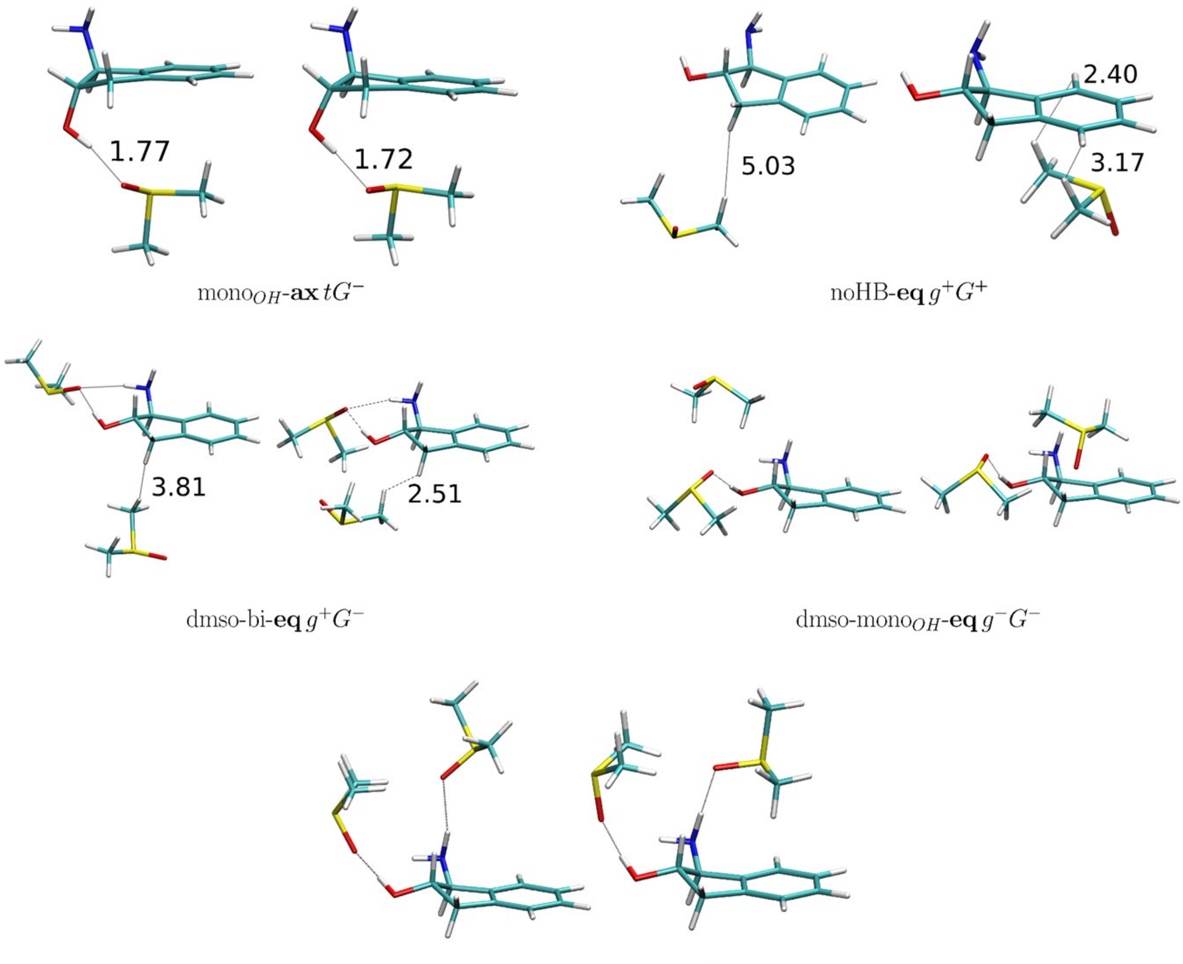

mono_{OH}-$\mathbf{ax}\,tG^{-}$

noHB-$\mathbf{eq}\,g^{+}G^{+}$

dmso-bi-$\mathbf{eq}\,g^{+}G^{-}$

dmso-mono_{OH}-$\mathbf{eq}\,g^{-}G^{-}$

mono_{OH}-mono_{NH}-$\mathbf{eq}\,g^{+}G^{-}$

Figure S3: Comparison between the geometry calculated at the B3LYP/6-311G++(d,p) level without (left) or with (right) dispersion correction for a selection of *trans*-AI:(DMSOd_6) 1:1 and *trans*-AI:(DMSOd_6)$_2$ 1:2 complexes.

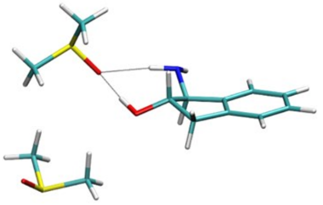

dmso-bi-$\mathbf{eq}\,g^{+}T$: 1.6 kJ·mol^{-1}

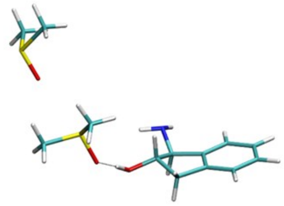

dmso-mono$_{OH}$-$\mathbf{eq}\,g^{-}T$: 2.3 kJ·mol^{-1}

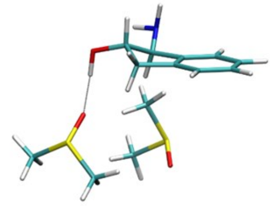

dmso-mono$_{OH}$-$\mathbf{eq}\,tG^{-}$: 3.1kJ·mol^{-1}

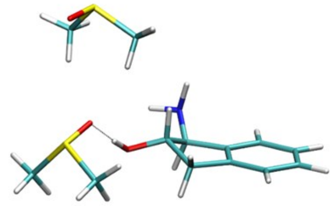

dmso-mono$_{OH}$-$\mathbf{eq}\,g^{-}G^{-}$: 4.9 kJ·mol^{-1}

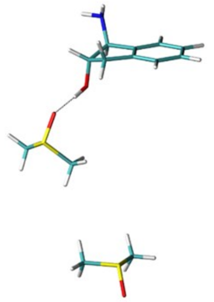

dmso-mono$_{OH}$-$\mathbf{ax}\,g^{-}G^{-}$: 6.6kJ·mol^{-1}

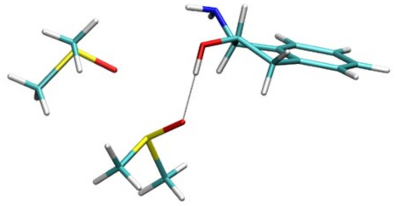

dmso-mono$_{OH}$-$\mathbf{eq}\,tT$: 6.4 kJ·mol^{-1}

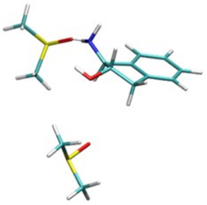

dmso-mono$_{NH}$-$\mathbf{eq}\,g^{+}G^{+}$: 6.9kJ·mol^{-1}

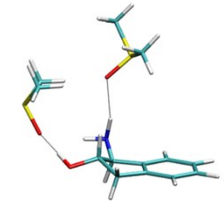

mono$_{OH}$-mono$_{NH}$-$\mathbf{eq}\,g^{+}G^{-}$: 8.3kJ·mol^{-1}

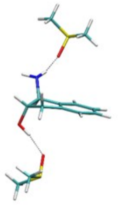

mono$_{OH}$-mono$_{NH}$-$\mathbf{ax}\,tT$: 15.7 kJ·mol^{-1}

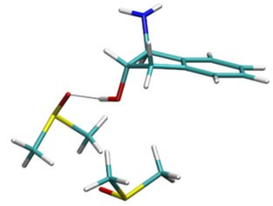

dmso-mono$_{OH}$-$\mathbf{ax}\,g^{+}T$: 16.9kJ·mol^{-1}

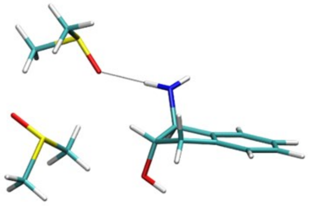

dmso-mono$_{NH}$-$\mathbf{ax}\,tT$: 29.4 kJ·mol^{-1}

Figure S4: Stable calculated structure of the *trans*-AI:(DMSOd_6)$_2$ 1:2 complex at the B3LYP/6-311G++(d,p) level in a DMSO continuum.

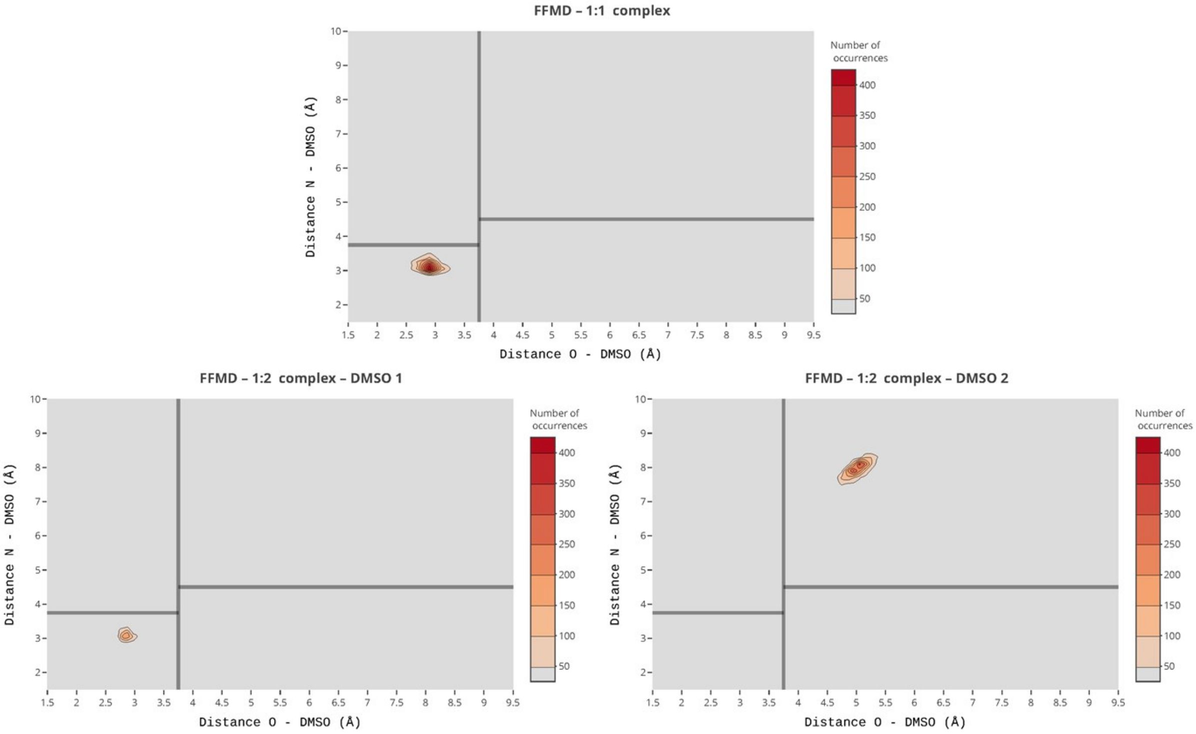

Figure S5: Contour plots of occurrence of O(*trans*-AI)-DMSO and N(*trans*-AI)-DMSO distances in the *trans*-AI:(DMSO) 1:1 and *trans*-AI:(DMSO)$_2$ 1:2 equatorial complexes at 150 K in FFMD simulations.

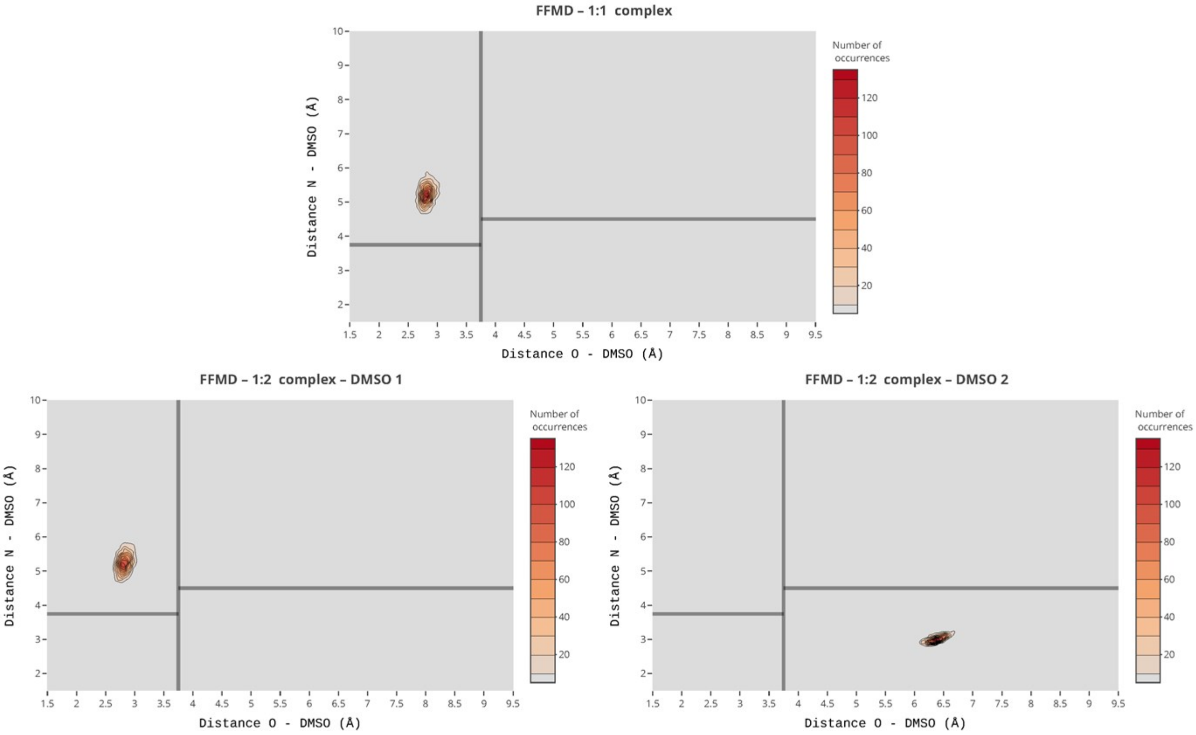

Figure S6: Contour plots of occurrence of O(*trans*-AI)-DMSO and N(*trans*-AI)-DMSO distances in the *trans*-AI:(DMSO) 1:1 and *trans*-AI:(DMSO)$_2$ 1:2 axial complexes at 150 K in FFMD simulations.

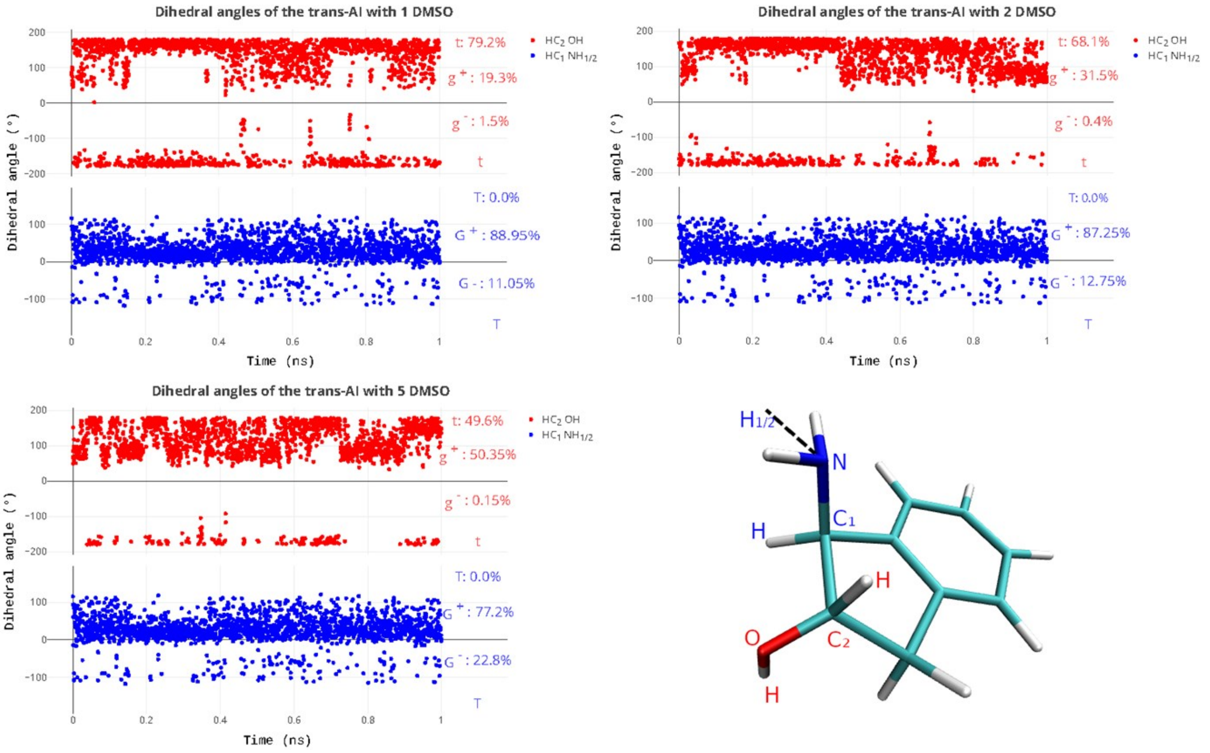

Figure S7: Dihedral angles describing the geometries of the hydroxyl (red) and amino groups (blue) of *trans*-AI during the FFMD simulations at 300 K with one, two and five DMSO.

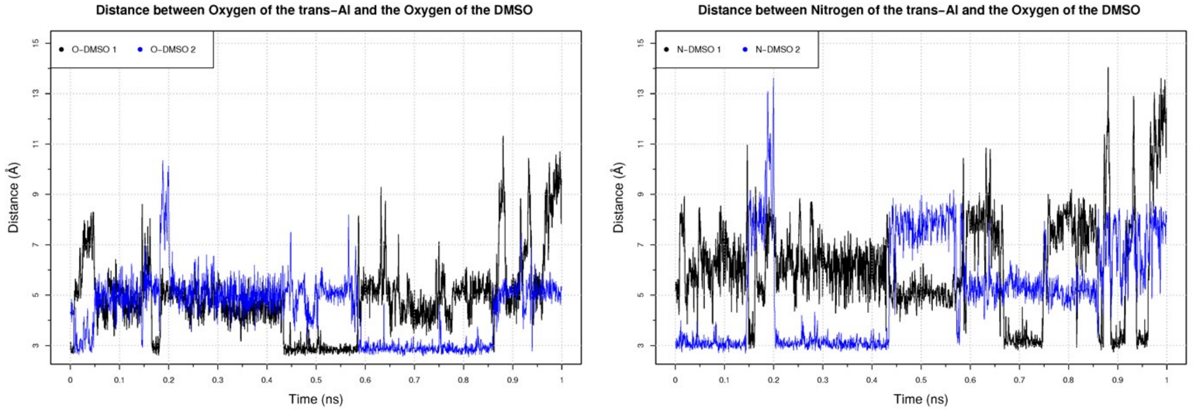

Figure S8: Distances evolution as a function of time for the *trans*-AI:(DMSO)$_2$ 1:2 complex at 300 K, left: O(*trans*-AI)-O(DMSO), right: N(*trans*-AI)- O(DSMO).

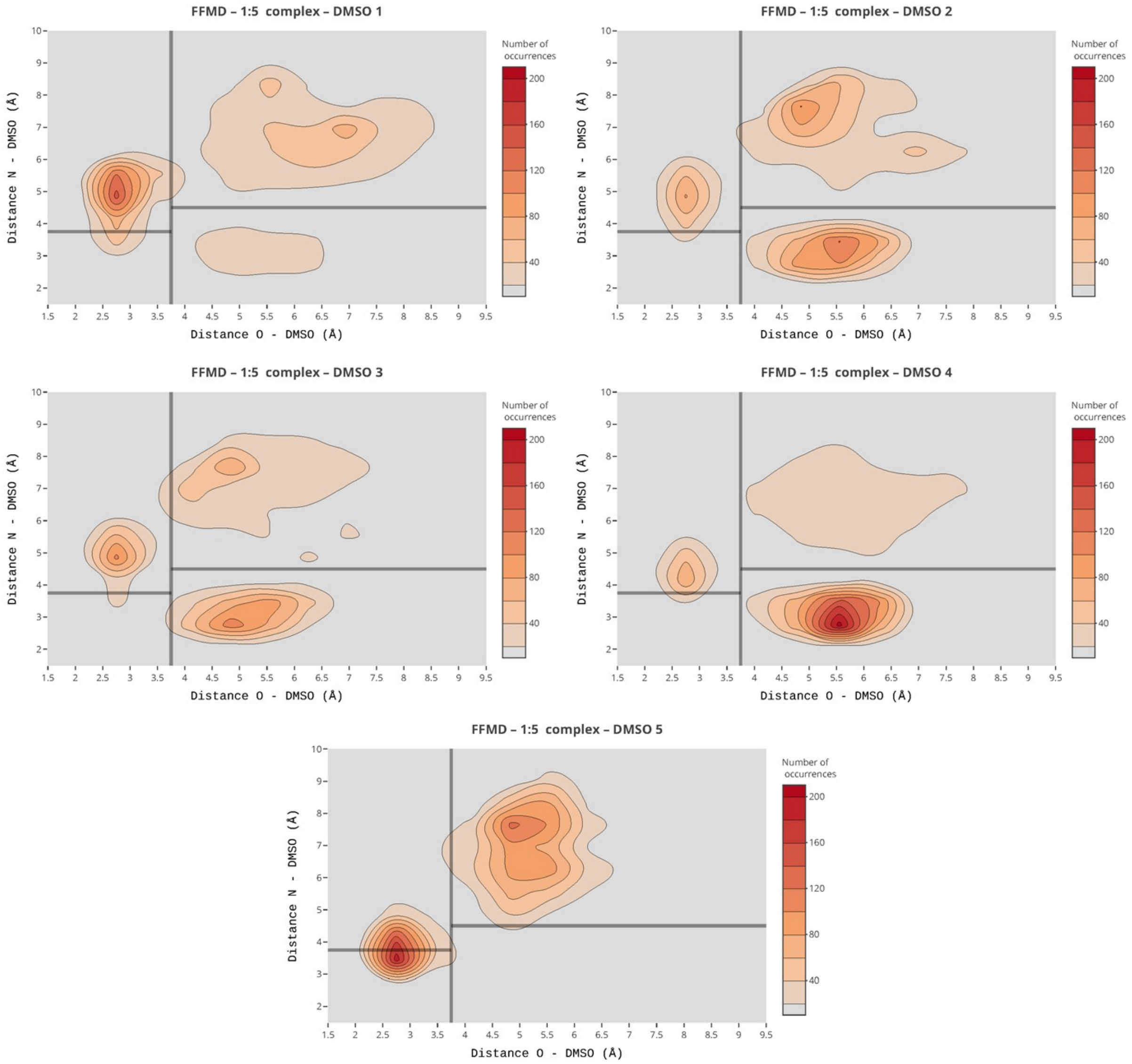

Figure S9: Contour plots of occurrence of O(*trans*-AI)-DMSO and N(*trans*-AI)-DMSO distances for the five DMSO molecules in the *trans*-AI:(DMSOd_6)$_5$ complex during the FFMD simulations at 300 K.

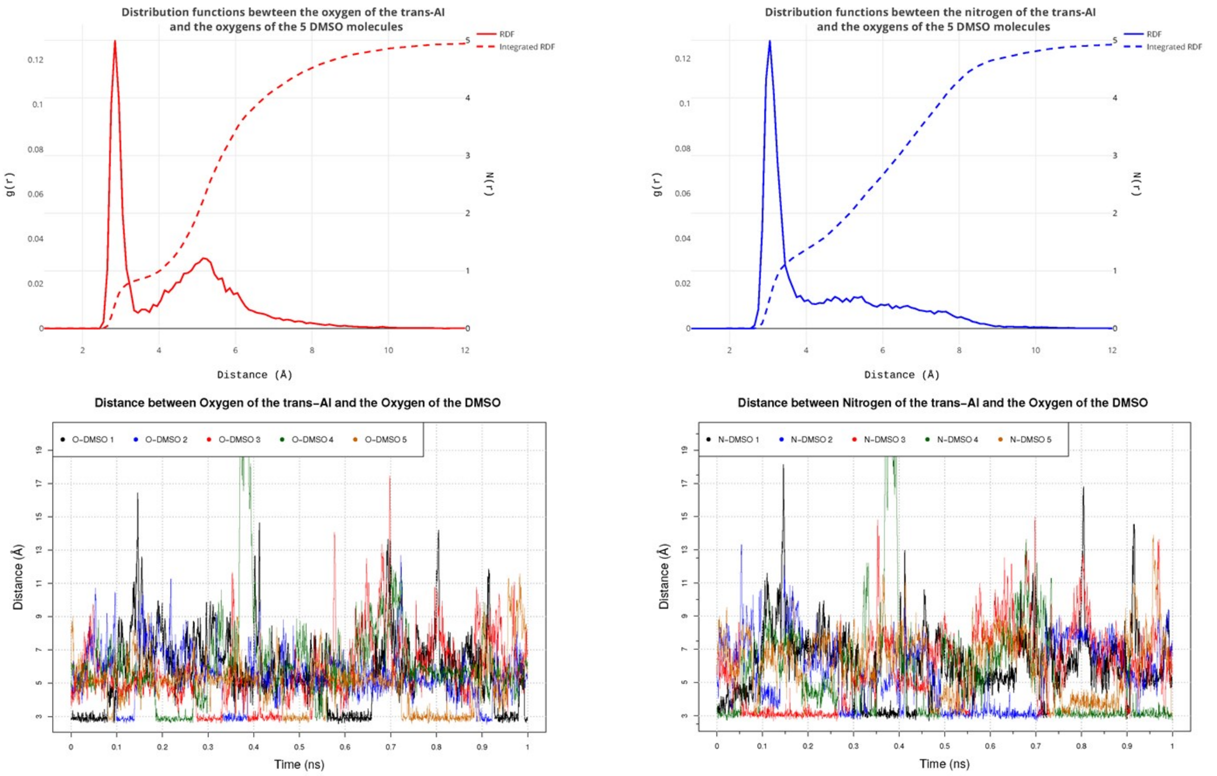

Figure S10: Radial distribution functions (RDF) (top) and distance evolution (bottom) as a function of time for the *trans*-AI:(DMSO)$_5$ 1:5 complex at 300 K, left: O(*trans*-AI)-O(DMSO), right: N(*trans*-AI)- O(DSMO).

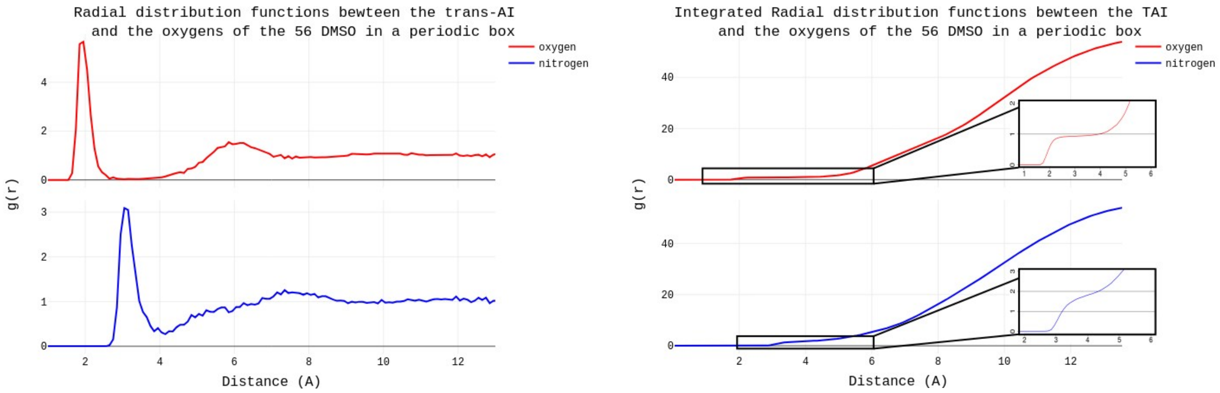

Figure S11: Radial distribution functions (RDF) for *trans*-AI in a box of 56 DMSO molecules at 300 K. The RDF between the oxygen of the *trans-AI* and the DMSO molecules (red) shows an intense peak at 2 Å while the RDF between the nitrogen and the DMSO molecules (blue) shows an intense peak at 3 Å.

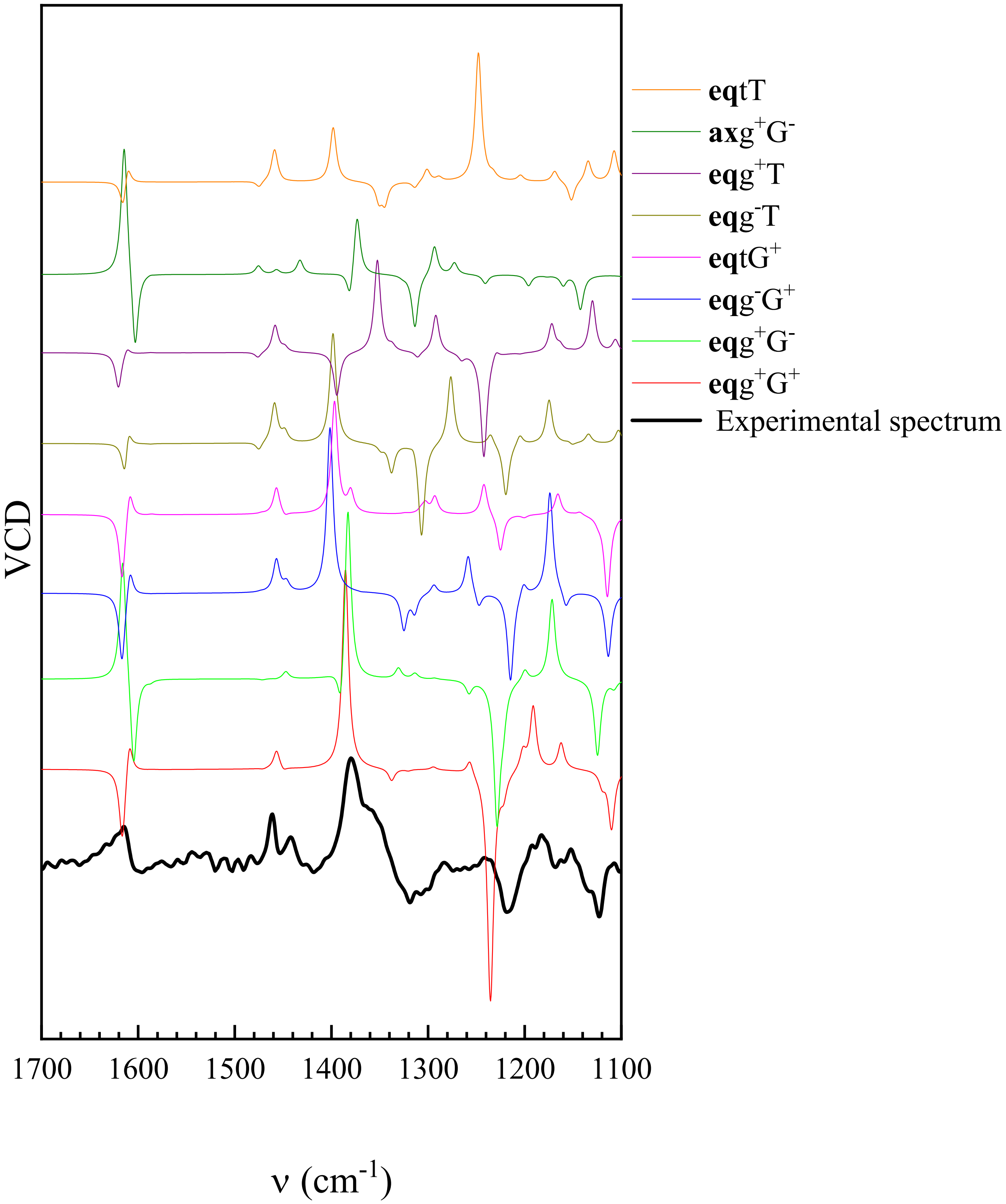

Figure S12: Simulated VCD spectra of the most stable conformers of (*S,S*)-*trans*-AI.

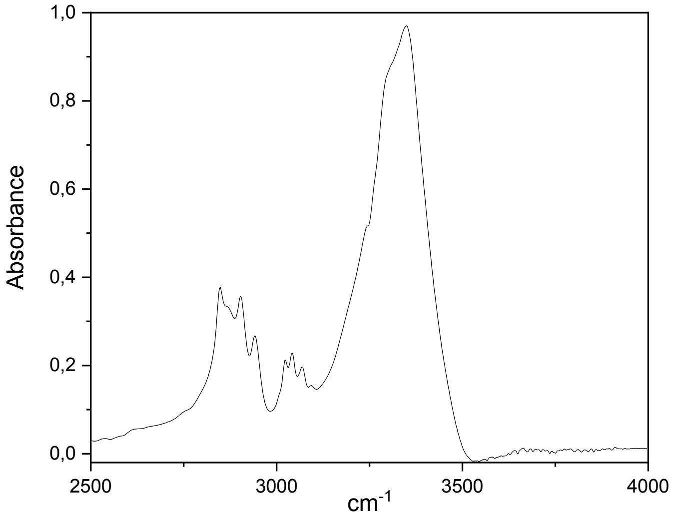

Figure S13: Absorption spectrum of *trans*-AI in a DMSO solution, in the 3 μm region.

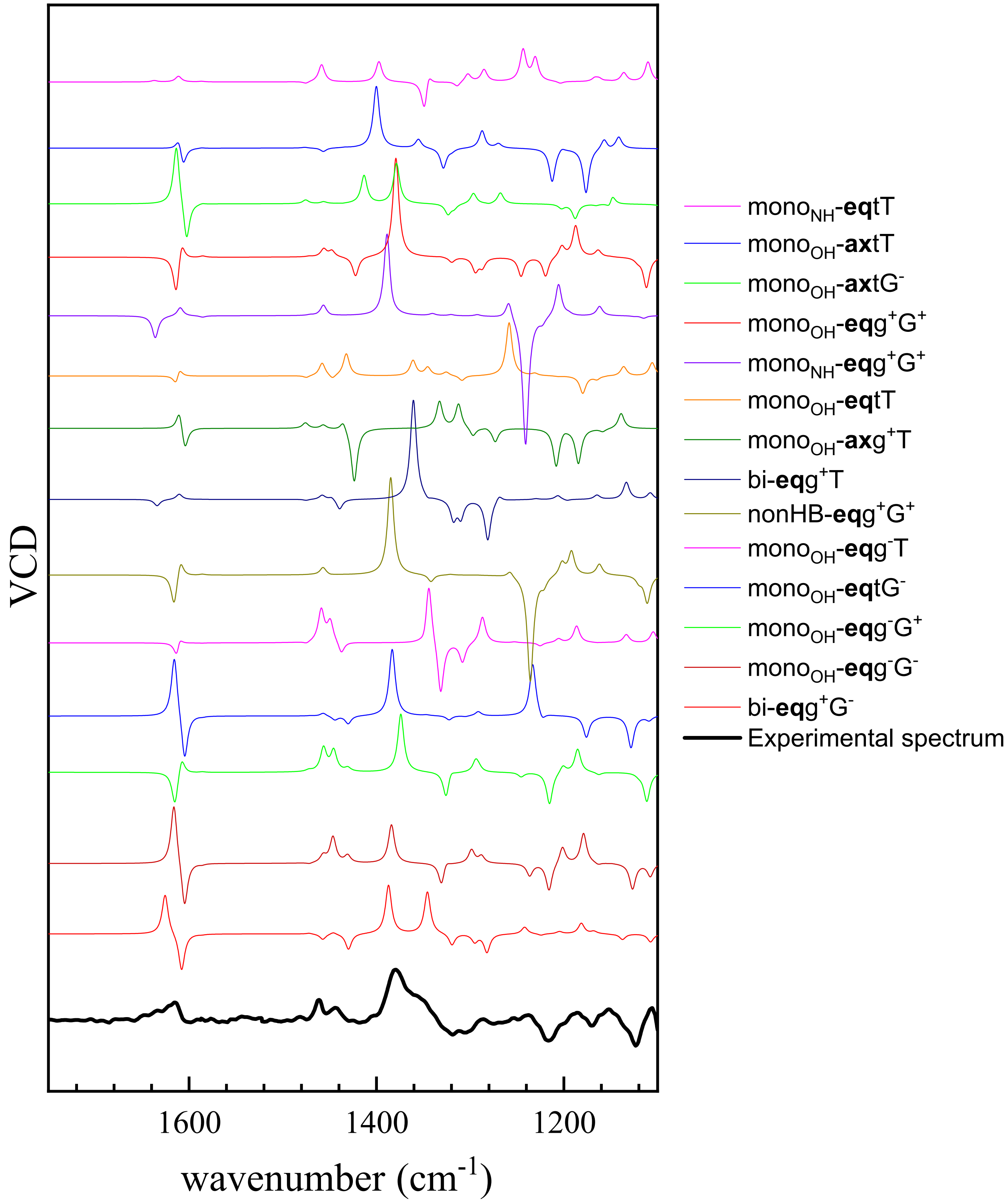

Figure S14: Simulated VCD spectra of the most stable conformers of the (*S,S*)-*trans*-AI:(DMSOd_6) 1:1 complexes in a DMSO continuum calculated at the B3LYP/6-311++G(d,p) level.

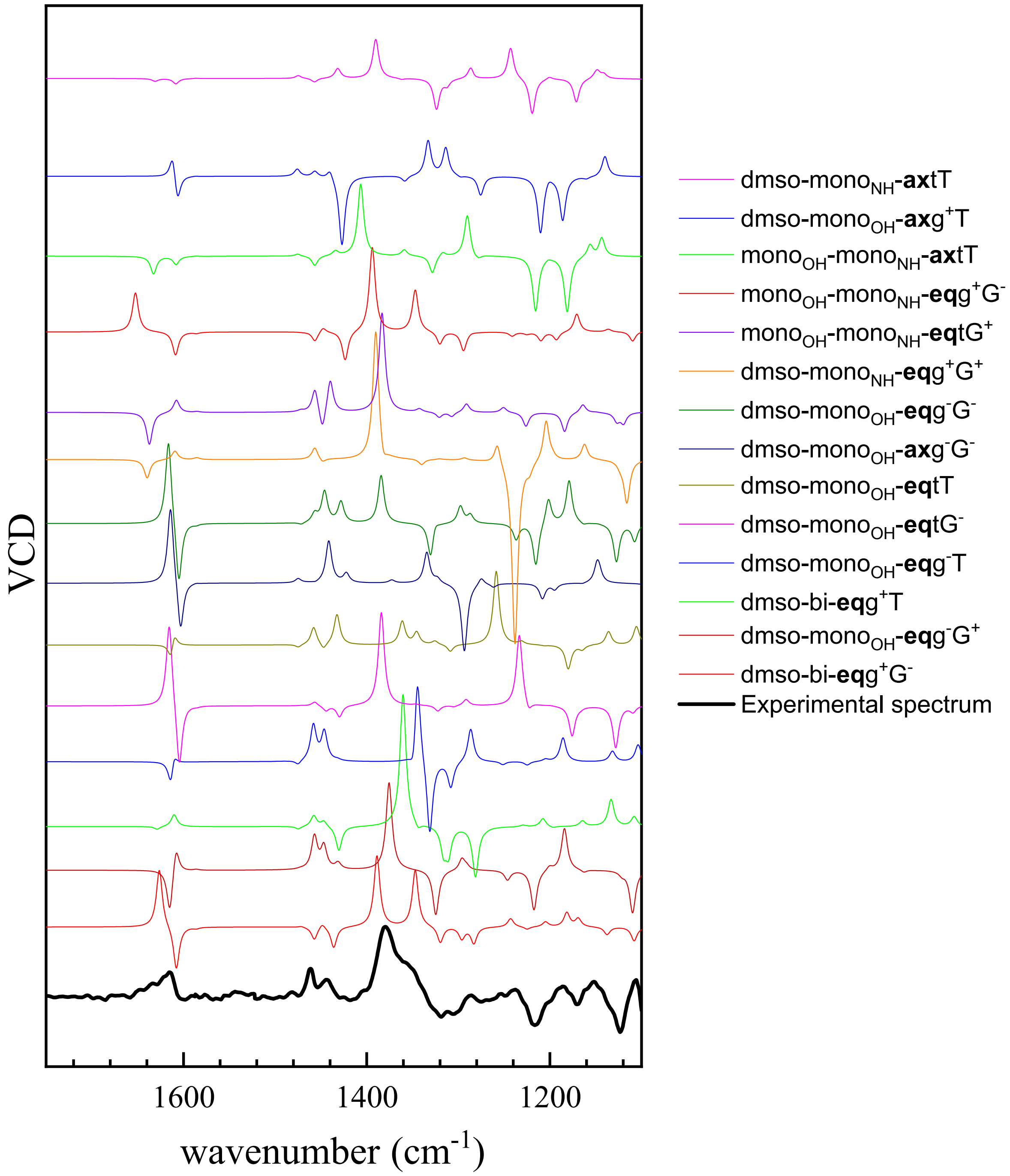

Figure S15: Simulated VCD spectra of the most stable conformers of the (*S,S*)*trans*-AI:(DMSOd_6)$_2$ 1:2 complexes in a DMSO continuum calculated at the B3LYP/6-311++G(d,p) level.

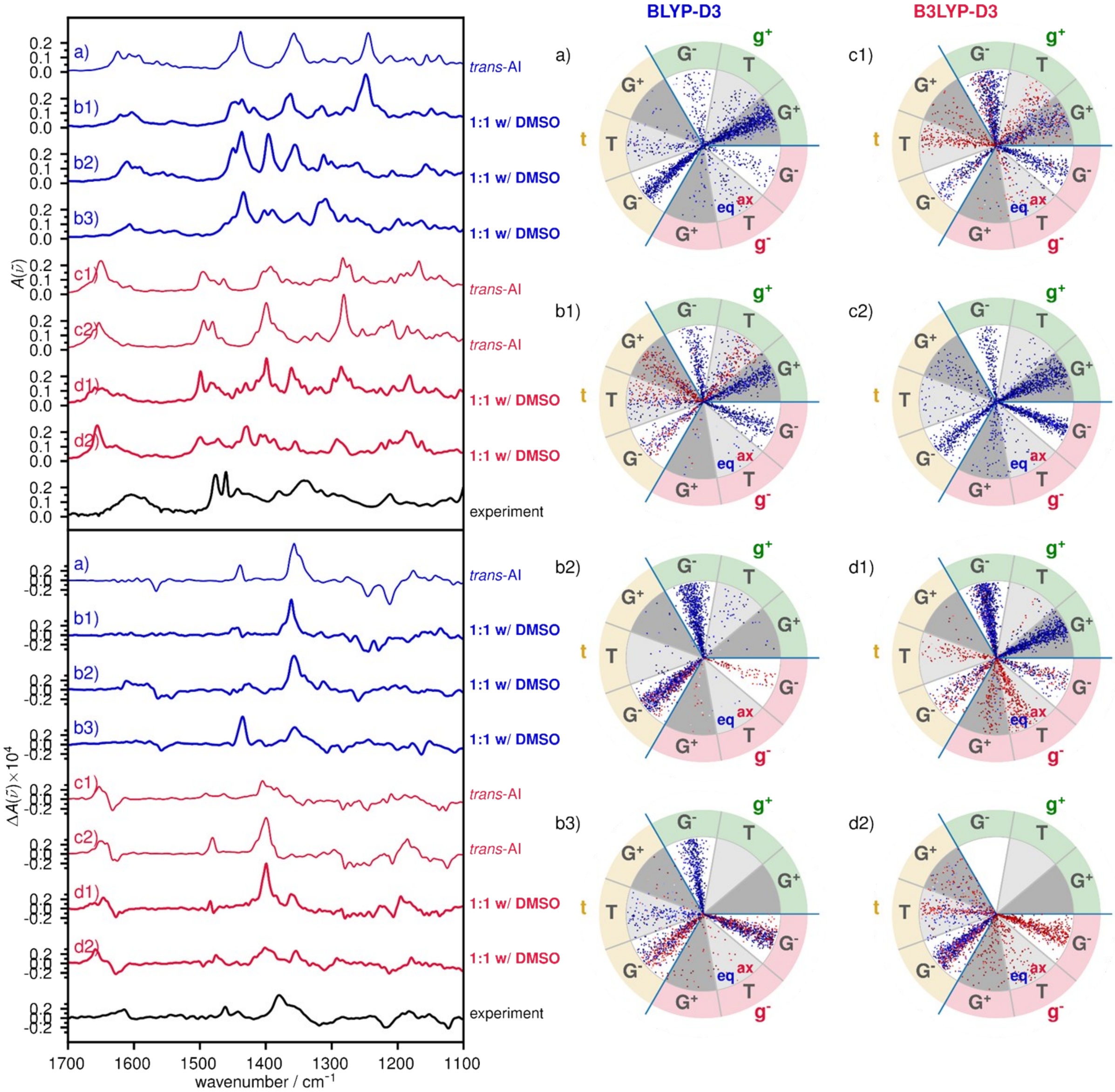

Figure S16: Left: IR and VCD spectra obtained for each individual FPMD BLYP trajectory (blue colour) used for the average presented in Figure 12, for the monomer (a) and the 1:1 complex (b_1 to b_3), together with sampling clocks (right). Same for B3LYP trajectories (red colour) for the monomer (c_1 to c_2) and the 1:1 complex (d_1 to d_2). Sampling clock (right), displaying how the conformational space of (*S,S*)-*trans*-AI is visited by each FPMD trajectory. The circle is divided in regions of OH orientation and sub-divided in regions of NH_2 orientation, using the notation of the static cluster analysis. The density of points is therefore proportional to the abundance of the corresponding conformation, whereas points in blue and red indicate equatorial and axial conformations, respectively.